

**Field Observations Reveal Substantially Higher Scattering-Refractive  
Index in Enhancement by Secondary Versus Primary Organic  
Aerosols**  
**Aerosol Formation in Humid Southern China Challenges  
Model Assumptions**

Junlin Shen<sup>1</sup>, Li Liu<sup>2</sup>, Fengling Yuan<sup>1</sup>, Biao Luo<sup>1</sup>, Hongqing Qiao<sup>1</sup>, Miaomiao Zhai<sup>1</sup>, Gang Zhao<sup>3</sup>,  
Hanbing Xu<sup>4</sup>, Fei Li<sup>5</sup>, Yu Zou<sup>2</sup>, Tao Deng<sup>2</sup>, Xuejiao Deng<sup>2</sup>, Ye Kuang<sup>1</sup>

<sup>1</sup> Institute for Environmental and Climate Research, College of Environment and Climate, Jinan  
University, Guangzhou, 511443, Guangdong, China

<sup>2</sup> Guangzhou Institute of Tropical and Marine Meteorology of China Meteorological Administration,  
GBA Academy of Meteorological Research, Guangzhou, 510640, China.

<sup>3</sup> Key Laboratory of Ecology and Environment in Minority Areas, Minzu University of China, National  
Ethnic Affairs Commission, Beijing, 100081, China

<sup>4</sup> School of Computer Science and Engineering, Sun Yat-Sen University, Guangzhou, 510275,  
Guangdong, China

<sup>5</sup> Xiamen Key Laboratory of Straits Meteorology, Xiamen Meteorological Bureau, Xiamen, 361012,  
Fujian, China

Correspondence: Ye Kuang (kuangye@jnu.edu.cn) and Li Liu (liul@gd121.cn)

28

29

30 **Abstract:**

31 Aerosol-radiation interactions play a crucial role in air pollution and climate change with  
32 scattering being the dominant process. The complex refractive index of organic aerosols is essential  
33 for accurately simulating these interactions, with the scattering capability is predominantly determined  
34 by the real part of the refractive index ( $m_r$ ). Prevailing models often assume a constant  $m_r$  for organic  
35 aerosols (e.g., 1.53 or 1.45) at different wavelengths or claim that  $m_r$  of primary organic aerosols  
36 (POA) is substantially higher than that of secondary organic aerosols (SOA) (e.g., 1.63 for POA and  
37 1.43 for SOA), largely due to a lack of direct measurements. This study employs direct measurements  
38 from the DMA-SP2 system to demonstrate a strong diameter dependence of dry state  $m_r$  at 1064 nm,  
39 closely associated with primary aerosol emissions and secondary aerosol formation. Source  
40 apportionment of aerosol size distributions reveals that the  $m_r$  of SOA is substantially higher than that  
41 of POA. Optical closure calculations, based on extensive dry state observations of aerosol scattering  
42 at 525 nm, size distributions, and chemical compositions, ~~confirm this finding~~ confirmed that SOA  
43 formation would enhance aerosol  $m_r$  substantially (from lower than 1.45 when POA dominates to  
44 higher than 1.55 when SOA dominates). These results challenge existing model assumptions. In  
45 addition, further analysis reveals  $m_r$  of SOA increases with oxidation level, which is contrary to  
46 results of most laboratory studies on evolution of  $m_r$  of SOA, which is likely associated with  
47 multiphase SOA formation. Our analysis recommends  $m_r$  values at 525 nm of 1.37 for POA and 1.59  
48 for SOA in urban regions with emissions and meteorological conditions similar to those at the  
49 observation site in Guangzhou, a city located in humid southern China. These findings underscore that  
50 current modeling practices may introduce substantial inaccuracies in estimating the radiative effects  
51 of organic aerosols.

52

## 1. Introduction

Aerosol-radiation interactions play a crucial role in air pollution and climate change. Atmospheric aerosols scatter and absorb solar radiation, which can alter the thermal structure of the atmosphere, the radiative energy balance of the Earth-atmosphere system, and affect atmospheric visibility. On one hand, aerosols influence the thermal structure of the surface and atmosphere, which affects the development of the atmospheric boundary layer (Zhong et al., 2019), thereby playing an important role in the evolution of pollution processes and air pollution. On the other hand, by scattering and absorbing solar radiation, aerosols can affect the radiative energy balance of the Earth-atmosphere system, impacting both local and global climates. Due to the complexity of atmospheric aerosol components, the direct radiative effect of aerosols (referred to as aerosol-radiation interactions in the latest IPCC report) is the second-largest source of error in accurately assessing anthropogenic climate forcings (IPCC, AR6, 2023) and is a significant factor limiting the accurate prediction of global climate change.

The inability to accurately characterize the complex refractive index of organic aerosols is one of the major sources of error in accurately simulating the direct radiative effects of aerosols (Redemann et al., 2000; Li et al., 2021; Tsigaridis and Kanakidou, 2018). Organic aerosols are a significant component of atmospheric aerosols, on average accounting for about 20-60% of submicron aerosols in most continental regions (Zhang et al., 2007), and in some areas, such as tropical rainforest regions, the organic proportion can be as high as 90% (Kanakidou et al., 2005). Therefore, organic aerosols are one of the main contributors to the direct radiative effects of aerosols and likely a major source of error in accurately assessing these effects (Moise et al., 2015). Compared to inorganic aerosols, the complex chemical composition of organic aerosols poses a core challenge to accurately quantifying their optical properties (Wu et al., 2021). Based on Mie scattering theory, the core parameters affecting aerosol optical properties in dry state are aerosol size and complex refractive index. In both climate models and atmospheric chemical transport models, the complex refractive index is a fundamental parameter for calculating key optical parameters such as the extinction coefficient, single scattering albedo, and asymmetry factor (Moise et al., 2015). The real part ( $m_r$ ) of the complex refractive index corresponds mainly to scattering properties, while the imaginary part corresponds mainly to absorption properties. The extinction of solar radiation by aerosols is determined by aerosol scattering and absorption with scattering being the dominant process (Moise et al., 2015), and accurately characterizing  $m_r$  of organic aerosols ( $m_{r,OA}$ ) is thus key to accurately simulating aerosol radiative effects (Li et al., 2021; McMeeking et al., 2005). The review by Tsigaridis and Kanakidou (2018) pointed out that existing models either treat  $m_{r,OA}$  as a constant or

86 treat  $m_r$  for POA and SOA ( $m_{r,POA}$  and  $m_{r,SOA}$ ) as constants. For example, Curci, et al. (2019) set  
87  $m_{r,POA}$  to 1.63 and  $m_{r,SOA}$  to 1.43 in their model.

88 However, results from existing literature of laboratory studies demonstrate that  $m_{r,OA}$  varies a lot.  
89 The advantage of laboratory studies is that they can produce aerosol systems containing only organic  
90 components, with a relatively narrow size range, allowing the retrieval of  $m_{r,OA}$  based on scattering  
91 or extinction measurements. Consequently, laboratory quantitative studies on  $m_{r,SOA}$  have been  
92 conducted broadly (Moise et al., 2015), while  $m_{r,POA}$  are rarely investigated. The results show that  
93 the  $m_{r,SOA}$  varies mainly in the range of 1.36-1.66, and the variation of  $m_{r,SOA}$  is closely related to its  
94 precursors and oxidation pathways (Moise et al., 2015; Kim et al., 2014; Lambe et al., 2013; He et al.,  
95 2018). For example, results of He et al. (2018) demonstrate that  $m_{r,SOA}$  first increase with the oxidation  
96 state parameter O/C and then decrease with O/C during the aging. Li et al. (2023b, 2023c) further  
97 developed a parameterization scheme for  $m_{r,SOA}$  based on O/C and H/C and validated it using  
98 laboratory experiment results, however, its applicability to POA and SOA on the basis of field  
99 measurements remains lacking. Overall, the difficulty in direct quantification of  $m_{r,OA}$  on the basis of  
100 field measurements has made the variation characteristics of  $m_{r,OA}$  in the atmosphere remain elusive.

101 In this study, using field measurements of aerosol refractive index, aerosol size distributions,  
102 aerosol scattering properties as well as aerosol chemical compositions, the remarkable difference in  
103  $m_{r,POA}$  and  $m_{r,SOA}$  is revealed, ~~which serves~~. It was found that SOA formation in the observation site  
104 would enhance substantially the  $m_r$ . These findings serve strong observational evidence that  $m_{r,SOA}$   
105 is much higher than  $m_{r,POA}$  in many regions and values for model settings of  $m_{r,POA}$  and  $m_{r,SOA}$  are  
106 recommended on the basis of observations.

## 107 2. Materials and Methods

### 108 2.1 Field measurements

109 In this study, we utilized datasets from two field campaigns conducted at Haizhu Wetland Park,  
110 Guangzhou, China. The first campaign lasted less than two months, from January 12 to February 27,  
111 2022, while the second was a longer-term campaign spanning approximately seven months, from July  
112 27, 2022, to February 28, 2023.

113 During the first campaign, we observed the particle number size distribution (PNSD) in a dry  
114 state ~~(relative humidity for indoor measurements was near 10%)~~, ranging from 13 nm to 800 nm,  
115 using a Scanning Mobility Particle Sizer (SMPS, model 3086 and particle counter 3776 from TSI)  
116 with a temporal resolution of 5 minutes. The  $m_r$  of BC-free aerosols with diameters of 235 nm, 270

域代码已更改

117 nm, 300 nm, 335 nm, 370 nm, and 400 nm were measured using the DMA-SP2 system (differential  
 118 mobility analyzer in tandem with single-particle soot photometer); ~~from Droplet Measurement~~  
 119 ~~Technologies, Boulder, Colorado (Schwarz et al., 2006)).~~ This measurement method for  $m_r$  was  
 120 previously proposed by Zhao et al. (2019c). To briefly explain the  $m_r$  measurement using the DMA-  
 121 SP2 system: the SP2 channels receive both scattering and incandescent signals from sampled aerosols.  
 122 For pure scattering aerosols, the peak of the scattering signal is positively correlated with aerosol  
 123 scattering ability, which is determined by aerosol size and  $m_r$  for spherical particles. ~~The scattering~~  
 124 ~~strength (S) at 1064 nm can be expressed as:~~ The scattering strength (S) at 1064 nm can be expressed  
 125 as (Zhao et al., 2019c):

$$126 \quad S = C \times I_0 \times \sigma \times (PF_{45^\circ} + PF_{135^\circ}),$$

127 Where  $I_0$  is the instrument's laser intensity, C is a constant determined by the instrument's response  
 128 characteristics,  $\sigma$  is the scattering coefficient of aerosols,  $PF_{45^\circ}$  and  $PF_{135^\circ}$  are the scattering phase  
 129 functions at  $45^\circ$  and  $135^\circ$ , respectively. The relationship between the peak of the scattering signal and  
 130 the scattering strength of pure scattering aerosols has been calibrated using ammonium sulfate (see  
 131 Sect. S1 of the supplement). Consequently, the  $m_r$  at 1064 nm ( $m_{r1064}$ ) of SP2 laser for pure scattering  
 132 aerosols can be retrieved using the particle size from the DMA and the scattering strength from the  
 133 SP2, following the method demonstrated by Zhao et al. (2019c). The DMA-SP2 technique offers the  
 134 advantage of providing direct measurements of  $m_{r1064}$ . However, it also has certain limitations. For  
 135 instance, in this study, the  $m_{r1064}$  measurements are constrained to a diameter range of approximately  
 136 235 to 400 nm, depending on laser intensity, thereby excluding smaller particles (<200 nm) and  
 137 relatively larger submicron particles (>400 nm). Additionally, some BC-free particles exhibit  
 138 absorptive properties, such as brown carbon containing particles that may absorb at infrared  
 139 wavelengths (Hoffer et al., 2017). Thus, these particles may absorb laser energy during scattering  
 140 measurements, causing heating that can lead to the evaporation of semi-volatile or even low-volatile  
 141 species from the particle phase, potentially biasing the  $m_{r1064}$  measurements, ~~although~~. Although this  
 142 effect is likely very small because this type of brown carbon aerosols likely account for very small  
 143 portions of BC-free aerosols (Luo et al., 2022). Non-refractory submicron (NR-PM<sub>1</sub>) aerosol chemical  
 144 compositions—including ammonium (NH<sub>4</sub>), nitrate (NO<sub>3</sub>), sulfate (SO<sub>4</sub>), chloride (Cl), and organic  
 145 components—were measured using a Quadrupole Aerosol Chemical Speciation Monitor (Q-ACSM).  
 146 Aerosol absorptions at multiple wavelengths were measured using the AE33 from MAGEE (Drinovec  
 147 et al., 2015). Note that a PM<sub>2.5</sub> inlet (BGI, SCC 2.354) with a required flow rate of 8 L/min was used  
 148 for aerosol sampling, with a Nafion drier of 1.8 m length downstream of the impactor, which ensures  
 149 the sampling RH in instruments could be down to around 10% as recorded by the inlet RH sensor of

the Q-ACSM. The flow rates of the Q-ACSM, SMPS, SP2 and AE33 instruments were set to 3 L/min, 0.3 L/min, 0.1 L/min, and 5 L/min, respectively. Nafion drier and all sampling tubes before instruments were placed vertically to reduce sampling loss. Details about the quality assurance of Q-ACSM measurements during this campaign are provided by Li et al. (2023a).

During the second campaign, direct measurements of  $m_{r1064}$  were not conducted. ~~Instead, dry state aerosol scattering coefficients of total suspended particles (TSP) at 450, 525, and 635 nm were measured using a nephelometer under nearly dry conditions (below 15% relative humidity). The dry-state (relative humidity below 20%) PNSD, ranging from 13 to 800 nm, was again measured using the SMPS. Additionally, multi-wavelength aerosol absorption measurements were performed using an Aethalometer (AE33, (Drinovec et al., 2015)).~~ Instead, dry state aerosol scattering coefficients of total suspended particles (TSP) at 450, 525, and 635 nm were measured using a nephelometer (Aurora 3000 from Ecotech, (Müller et al., 2011)) under nearly dry conditions (below 15% relative humidity). The dry-state (relative humidity below 20%) PNSD, ranging from 13 to 800 nm, was again measured using the SMPS. Additionally, multi-wavelength aerosol absorption measurements were performed using an AE33 Aethalometer (Drinovec et al., 2015), and the NR-PM<sub>1</sub> aerosol chemical compositions were also measured using the Q-ACSM.

## 2.2 Source Analysis Methods of Organic Aerosols and Aerosol Size Distributions

The multilinear engine (ME-2) technique (Canonaco et al., 2013; Canonaco et al., 2021) was applied to the organic aerosol mass spectra to resolve the sources of organic aerosols. Multilinear Engine (ME-2) is an upgrade of widely used Positive Matrix Factorization (PMF) technique and runs on an IGOR-based interface (Canonaco et al., 2013). Different from traditional PMF, ME-2 offers capability of constraining the spectra variation extent of OA factor with given priori mass spectra (Canonaco et al., 2013; Guo et al., 2020). Four factors were identified across both field campaigns: two primary organic aerosol (POA) factors and two secondary organic aerosol (SOA) factors. The POA factors consisted of hydrocarbon-like organic aerosol (HOA) and cooking-like organic aerosol (COA), while the SOA factors consisted of less oxygenated organic aerosol (LOOA) and more oxygenated organic aerosol (MOOA). The spectral profiles of HOA and COA obtained in Liu et al. (2022) were used in the ME-2 procedure to constrain POA factor variations.

The POA factors exhibited consistent spectral profiles and elemental ratios between the two campaigns. For example, the O/C ratios of HOA were 0.16 and 0.17, and the O/C ratios of COA were 0.12 and 0.14, respectively. However, the resolved SOA factors differed between the campaigns. The O/C ratio of LOOA in the short-term campaign was 0.89, while it was 0.60 in the long-term campaign.

182 Similarly, the O/C ratio of MOOA was 0.93 in the short-term campaign and 1.27 in the long-term  
183 campaign. These differences do not affect the overall analysis of this study, as the focus is primarily  
184 on the distinction between POA and SOA. More details about the source analysis of organic aerosols  
185 can be found in the supplements of Li et al. (2023a) for the short-term campaign and Qiao et al. (2024)  
186 for the long-term campaign.

187 Additionally, following ~~the positive matrix factorization (PMF)~~ [PMF](#) procedure for the PNSD  
188 measurements and the source apportionment method introduced by Cai et al. (2020a), five PNSD  
189 factors were identified (PMF 2, ver. 4.2, 111 bins for PNSD ranging from 14 nm to 736 nm as inputs).  
190 For details on the determination of the factor numbers and the PNSD factor analysis, please refer to  
191 Sect. S2 of the supplement. In the source apportionment of PNSD factors, ammonium, nitrate, and  
192 sulfate measurements were paired as ammonium sulfate (AS) and ammonium nitrate (AN) using the  
193 scheme proposed by Gysel et al. (20) considering that different impacts of AS and AN formation on  
194 PNSD. The mass concentrations of refractory black carbon (rBC) during the short-term campaign were  
195 integrated from size-resolved rBC measurements obtained using the DMA-SP2 system, as described  
196 in Li et al. (2023a). Correlation analysis between mass concentrations of OA factors, rBC, AS as well  
197 as AN and resolved PNSD factors were performed to help explore sources of different PNSD factors.

198 In addition, the densities of aerosol species used for volume calculations in this study were  
199 consistent with those in Kuang et al. (2021): 1.78 g/cm<sup>3</sup> for AS and AN, 1.0 g/cm<sup>3</sup> for HOA and COA,  
200 1.2 g/cm<sup>3</sup> for LOOA, and 1.4 g/cm<sup>3</sup> for MOOA. However, 1.0 g/cm<sup>3</sup> was chosen for rBC on the basis  
201 of previous observations results (Zhang et al., 2016b; Zhao et al., 2020; Zhou et al., 2022). Calculating  
202 BC volume for hygroscopicity requires the material density of BC, as described in Kuang et al. (2021).  
203 However, for Mie calculations in this study, effective BC density is needed to determine the BC core  
204 size. Since the presence of air voids (Zhang et al., 2016b; Zhao et al., 2020) within BC particles  
205 increases their apparent size compared to calculations based on the material density. The source  
206 analysis of resolved PNSD factors through combination of ACSM measurements was discussed  
207 comprehensively in Sect 3.1 to help explore observed  $m_r$  diameter dependence.

### 208 **2.3 Optical Closure and associated $m_r$ Retrieval**

209 During the second long-term field campaign, dry-state aerosol scattering coefficients of TSP and  
210 PNSD (ranging from 13 to 800 nm, generally covering dry-state PM1), as well as ~~black carbon (BC)~~  
211 mass concentrations, were simultaneously measured, making it feasible to perform a closure between  
212 the measured and simulated aerosol scattering ( $\sigma_{sp,obs}$  vs  $\sigma_{sp,sim}$ ). Details about aerosol scattering  
213 calculating procedures and simulations using the Mie code of BHCOAT (Bohren and Huffman,

1998;Cheng et al., 2009) could be found in Sect. S4. Five key issues needed to be addressed for this closure: (1) The size range mismatch between aerosol scattering measurements (TSP) and PNSD measurements (dry-state PM<sub>1</sub>); (2) BC mass size distributions and mixing state, and other BC related parameters such as density and refractive index; (3) The  $m_r$  of BC-free aerosols at 525 nm; (4) Imaginary part of BC-free aerosols which is mostly associated with brown carbon; (5) Corrections for integrating nephelometer measurements to account for truncation errors and light source non-idealities (Müller et al., 2011).

Recent field observations (detailed in Sect. S3 of the supplement), utilizing a system (Kuang et al., 2024) that coupled different aerosol inlets with a integrating nephelometer, demonstrated that in Guangzhou's urban area, scattering coefficients of dry-state PM<sub>1</sub> and TSP ( $\sigma_{sp,PM_1}$  vs  $\sigma_{sp,TSP}$ ) generally agree well (Fig. S4a, R = 0.99). However, their ratio varies substantially depending on aerosol scattering levels (Fig. S4b). Specifically, the ratio  $\sigma_{sp,TSP}/\sigma_{sp,PM_1}$  at 525 nm exceeds 1.2 when  $\sigma_{sp,TSP}$  is below 50 Mm<sup>-1</sup>, reaching approximately 1.5 when  $\sigma_{sp,TSP}$  is around 10 Mm<sup>-1</sup>. This ratio decreases as  $\sigma_{sp,TSP}$  increases and stabilizes (near 1.08) when  $\sigma_{sp,TSP}$  exceeds 90 Mm<sup>-1</sup>. Consequently, for the closure, measured dry-state  $\sigma_{sp,TSP}$  was corrected to dry-state  $\sigma_{sp,PM_1}$  using the observed  $\sigma_{sp,TSP}$ -dependent relationship shown in Fig. S4b (ratio of 1.08). This ratio may vary across seasons. However, aerosol scattering simulation results based on particle size distribution measurements that cover the supermicron range, conducted during six campaigns across various locations and seasons in the North China Plain, indicate that PM<sub>1</sub> on average contributes approximately 90% to TSP scattering (Fig. 2 of Kuang et al. (2018)). This aligns closely with the average ratio of 1.08 determined in this study through direct scattering measurements, suggesting that this ratio likely does not vary substantially.

The BC mass size distributions and mixing state during the first short-term campaign were analyzed systematically in a previous study conducted by Li et al. (2023a). Two key findings emerged: (1) BC mass size distributions for diameters >100 nm could be represented by a single lognormal mode, with a geometric mean diameter ( $D_g$ ) of 258 (±16) nm and a geometric standard deviation ( $\sigma_g$ ) of 1.69; (2) Nearly half of the BC mass was identified as externally mixed. The mass fraction of externally mixed BC in total BC ( $R_{ext}$ ) was calculated as  $0.56 \pm 0.16$ , and the number fraction ( $R_{csm}$ ) of internally mixed BC (represented by the core-shell model) in total number of internally mixed BC and BC-free particles was  $0.13 \pm 0.12$ . These findings indicated that, despite clear evidence of secondary aerosol formation during the first campaign, BC mass size distributions and mixing states varied within a relatively narrow range, primarily influenced by traffic emissions (Li et al., 2023a). Therefore, the



246 parameters  $D_g = 258$  nm,  $\sigma_g = 1.69$ ,  $R_{ext} = 0.56$ , and  $R_{csm} = 0.13$  were used to distribute the BC mass  
 247 concentrations measured by the AE33 and account for BC mixing states. In brief, aerosol particles were  
 248 divided into three types: externally BC, internally mixed BC with BC as the core, and BC-free. BC  
 249 mass was distributed into different diameters using the established lognormal function, and further  
 250 allocated to externally and internally mixed BC-containing particles using parameters  $R_{ext}$  and  $R_{csm}$ .  
 251 Note that these values regarding BC size distributions and mixing states are not expected to remain  
 252 constant throughout the campaign. However, sensitivity test conducted on the basis of observations in  
 253 the short campaign help boost the confidence. Sensitivity test results shown in Fig.S5 show that even  
 254 if the geometric mean diameter of the BC mass size distribution changes from 180 nm to 600 nm, very  
 255 large variation according to reported distribution in literatures (Zhao et al., 2019b), the relative changes  
 256 in scattering calculations remain relatively small ( $\sim 2\%$ ). Instead, the BC mixing state plays a more  
 257 critical role. For example, changing the mixing state from completely externally mixed to a fully core-  
 258 shell internal mixture results in changes of approximately 10%. However, such a scenario represents  
 259 an extreme condition. Considering the observation site is located near BC source regions, BC aerosols  
 260 are likely closer to being externally mixed. Errors associated with the BC mixing state parameter are  
 261 estimated to be less than 2.5%. This inference assumes that BC mixing states in this region vary from  
 262 completely externally mixed to half externally mixed (much larger than observed in the first short  
 263 campaign). Using an average value in this case would result in uncertainties of less than 2.5%. Errors  
 264 associated with BC mixing state would likely be smaller. In addition, other BC related parameters  
 265 might also induce retrieval errors, such as uncertainties associated with BC density, BC mass and BC  
 266 refractive index. Especially, the BC mass concentrations derived from AE33 measurements would  
 267 bear uncertainties associated with variations in mass absorption coefficient (Zhao et al., 2021b).  
 268 Sensitivity tests about these parameters are also included in Fig.S5. Results of previous study reveal  
 269 the refractive index of BC has almost minimal impact on scattering calculations (Ma et al., 2012a).  
 270 This is confirmed by the sensitivity test results shown in Fig. S5, with variations in possible reported  
 271 ranges of BC refractive index induce variations less than 2%. Results also show that uncertainties in  
 272 BC mass concentrations and BC density would only induce small scattering changes (near or less than  
 273 1%).

274 Note that, the sensitivity results shown here is somehow contrary to the conclusion draw by  
 275 Zhao et al. (2019b) that BC mass size distributions should have comparable impacts with BC mixing  
 276 states on simulations of aerosol scattering. This was further explored in Sect. S5. The results  
 277 demonstrate that the simulations in Zhao et al. (2019b) assumes all aerosols contain BC, which is  
 278 not the case in ambient atmosphere, details about this discussion could be found in Sect. S5.

In this region, both primary and secondary aerosols contribute to aerosol absorption (Yuan et al., 2016; Luo et al., 2022), which affect imaginary refractive index part ( $m_i$ ) of BC-free aerosols. The sensitivity tests about impacts of  $m_i$  on scattering calculations were also included in Fig.S5. It shows that varying  $m_i$  from  $10^{-2}$  to  $10^{-7}$  (reported  $m_i$  for different types of brown carbons (Saleh, 2020)) could result in scattering changes of  $\sim 5\%$ . However, even for biomass burning organic aerosols which are the most absorbing aerosol type, their  $m_i$  at 525 nm is on the order of  $10^{-2}$ . The BC-free aerosols during this campaign mostly consist of inorganic and secondary organic aerosols. The overall  $m_i$  of BC-free aerosols are less than  $10^{-3}$  estimated using the brown carbon absorption at 520 nm observed during the campaign even when biomass burning activities prevail (Luo et al., 2022), meaning that scattering deviations induced by errors  $m_i$  in assumption are less than 1% for assuming  $m_i$  of  $10^{-7}$ .

Truncation errors and light source non-idealities were accounted for in the Mie calculations by applying angular light intensity correction functions from Müller et al. (2011). Details of the Mie theory calculations for the optical closure can be found in Sect. S4 of the supplement. Sensitivity tests (discussed in Sect. 5 of the supplement) and above-mentioned discussions make it clear that  $m_r$  is the most influential parameter affecting the variations in aerosol scattering calculations.

Therefore, the optical closure calculations could be conducted iteratively to retrieve an  $m_r$  value that align simulated aerosol scattering at 525 nm with the measured scattering at the same wavelength (Sect. S4). This retrieved  $m_r$  at 525 nm, obtained through optical closure, is termed  $m_{rc525}$ . The sensitivity tests results shown in Fig.S7 demonstrate the accuracy of  $\sigma_{sp,PM_1}$  conversion from represents one of the most important factors that would influence the accuracy of retrieved  $m_{rc525}$ . The accuracy of  $\sigma_{sp,PM_1}$  depends largely on the accuracy of ratio used for converting measured  $\sigma_{sp,TSP}$  to  $\sigma_{sp,PM_1}$  as discussed. Large standard deviation of the ratio  $\sigma_{sp,TSP}/\sigma_{sp,PM_1}$  ( $>10\%$ ) exist for data points of  $\sigma_{sp,TSP}$  at 525 nm below  $50 \text{ Mm}^{-1}$  (shown in Fig. S4b). For these points, even if correcting the inlet inconsistency with the average curve shown in Fig.S4, large uncertainty would inevitably be introduced to the optical closure. Therefore,  $m_{rc525}$  was only retrieved when  $\sigma_{sp,TSP}$  at 525 nm exceeded  $50 \text{ Mm}^{-1}$  ( $\sim 75\%$  of data points), where the ratio between  $\sigma_{sp,PM_1}$  and  $\sigma_{sp,TSP}$  varied with standard deviations less than 5% (Fig.S4).

306

### 307 3 Results and discussions

#### 308 3.1 Strong Diameter Dependence of $m_{r1064}$ and Remarkable Difference in $m_{r,POA}$ and $m_{r,SOA}$ 309 Revealed by Direct $m_{r1064}$ Measurements

During the first campaign, significant variations in the  $m_{r1064}$  were revealed using DMA-SP2 measurements (Fig. S9), with  $m_{r1064}$  values ranging from 1.40 to 1.59 (mean:  $1.49 \pm 0.03$ ). Fig. 1a and 1b illustrate the diameter-dependent characteristics of the measured  $m_{r1064}$ . Aerosols larger than 300 nm generally exhibited higher  $m_{r1064}$  values compared to those smaller than 300 nm, with average  $m_{r1064}$  values at diameters of 253 nm, 270 nm, 300 nm, 335 nm, 370 nm, and 400 nm being 1.46, 1.49, 1.48, 1.51, 1.51, and 1.51, respectively. This is consistent with previous findings indicating a clear diameter dependence, where  $m_{r1064}$  tends to increase with particle diameter (Benko et al., 2009; Zhao et al., 2019a). Using the  $m_{r1064}$  ratio between 400 nm and 235 nm ( $m_{r1064,400}/m_{r1064,235}$ ) as an indicator of  $m_{r1064}$  diameter dependence, we found that this ratio increases with  $m_{r1064,400}$  (Fig. 1b). Specifically, the ratio  $m_{r1064,400}/m_{r1064,235}$  rose from 1.02 to 1.07 as  $m_{r1064,400}$  increased from 1.46 to 1.58, while  $m_{r1064,235}$  showed only a slight increase from 1.45 to 1.47. This suggests that the chemical processes responsible for the increase in  $m_{r1064,400}$  have minimal influence on the chemical properties of aerosol particles near 235 nm, ~~indicating~~. Indicating that variations in  $m_{r1064,400}$  and  $m_{r1064,235}$  are governed by different chemical and emission processes. The aerosol chemical compositions of NR-PM<sub>1</sub> presented in Fig. 1b reveal that the condition corresponding to  $m_{r1064,400}$  of 1.56 has an overall higher content of MOOA than that near  $m_{r1064,400}$  of 1.48. This is further confirmed by the probability distribution of MOOA mass fractions in two regions of Fig. 1b shown in Fig. S10. Although size distribution of secondary aerosols matter, this general result suggests that secondary organic aerosol formation has possibly contributed to the substantial increase in  $m_{r1064,400}$ . However, these results reflect bulk compositional changes that may differ considerably from changes in composition fractions at 400 nm. Overall, these findings indicate that aerosols with diameters near

235 nm and 400 nm likely originate from distinct sources, and variations in  $m_{r1064,235}$  and  $m_{r1064,400}$  might reveal  $m_r$  characteristics of different aerosols sources.

As introduced in the previous section, the PMF source apportionment technique was applied to aerosol chemical composition measurements and aerosol volume size distribution measurements derived from PNSD measurements during the first short-term field campaign. Results of these two approaches were combined to resolve the chemical fingerprints of sources at different diameters. Fig. 2a illustrates the average volume size distributions of five resolved factors based on PNSD measurements. It shows that aerosols at a diameter of 235 nm are primarily contributed by factors 1, 2, and 5, with factor 2 being the most significant contributor. In contrast, aerosols at 400 nm are mainly contributed by factors 1, 2, and 3, with factor 1 as the dominant contributor. As detailed in Sect. 2.2,

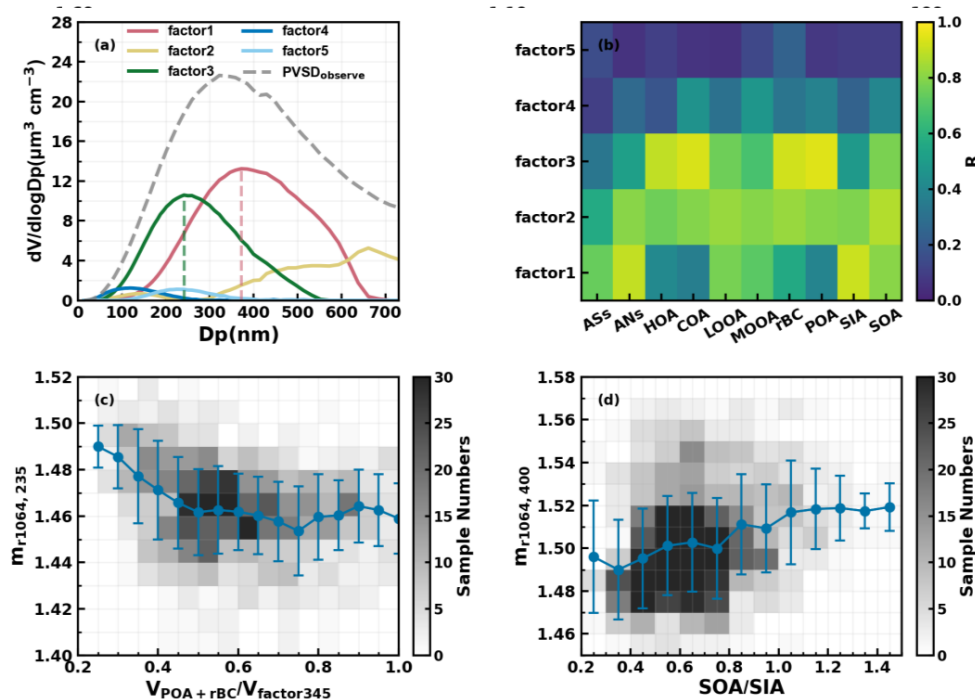


**Figure 2.** (a) The volume size distributions of factors from PNSD PMF analysis; (b) Correlation coefficient between volume concentrations of chemical compositions and resolved PNSD size factors; (c)  $m_{r1064,235}$  varies with changes in the ratio of volume sum of POA and rBC to the volume sum of factor3, factor4 and factor5 (factor 345); (d)  $m_{r1064,400}$  varies with SOA to SIA when mass summation of factor1 and factor 2 account for over 70% at 400 nm. The intensity of colors indicates the numbers of samples, while red spots and error bars represent average values and standard deviations in (c) and (d).

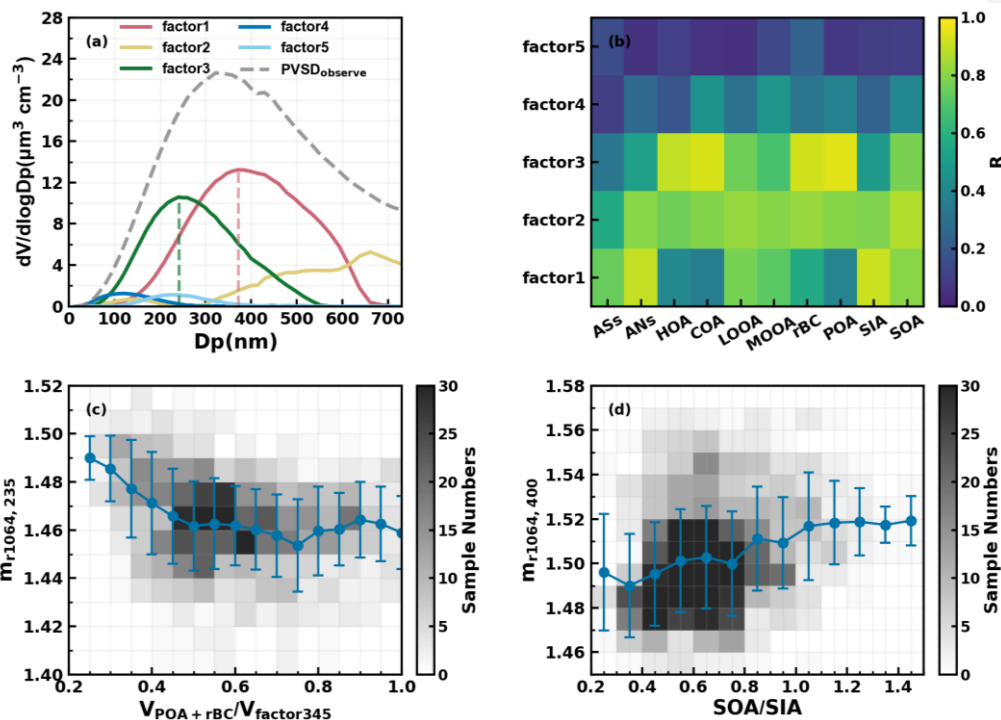


**Figure 2.** (a) The volume size distributions of factors from PNSD-PMF analysis; (b) Correlation coefficient between volume concentrations of chemical compositions and resolved PNSD size factors; (c)  $m_{1064,235}$  varies with changes in the ratio of volume sum of POA and rBC to the volume sum of factor3, factor4 and factor5 (factor 345); (d)  $m_{1064,400}$  varies with SOA to SIA when mass summation of factor1 and factor2 account for over 70% at 400 nm. The intensity of colors indicates the numbers of samples, while red spots and error bars represent average values and standard deviations in (c) and (d).

demonstrating a dominant contribution from secondary sources. Fig.2a illustrates the average volume size distributions of five resolved factors based on PNSD measurements. It shows that aerosols at a diameter of 235 nm are primarily contributed by factors 1, 3, and 5, with factor 3 being the most significant contributor. In contrast, aerosols at 400 nm are mainly contributed by factors 1, 2, and 3, with factor 1 as the dominant contributor, demonstrating a dominant contribution from secondary sources.

Cai et al. (2020a) introduced an analytical method linking resolved aerosol size distributions to different sources obtained from mass spectrometer measurements; this method is adopted here. The correlation coefficients for mass concentrations of different aerosol sources and volume of different factors are shown in Fig.2b. For factor 1, the volume peak size is around 400 nm, contributing an average of 58% to the total measured aerosol volume, and shows a strong correlation with secondary inorganic aerosols (SIA,  $R = 0.91$ ), as well as a notable correlation with SOA ( $R = 0.80$ ). Factor 2 contributes an average of 5.61% to the total volume and exhibits the highest correlation with SOA ( $R = 0.87$ ). The correlation analysis indicates that factors 1 and 2 are indeed linked to secondary sources, with the correlation coefficient between the volume sums of factors 1 and 2 and the mass concentrations of secondary components (SIA + SOA) reaching as high as 0.95. Taken together, these findings suggest that secondary organic and inorganic particulate matter are dominant components in particles larger than 400 nm, consistent with previous observations that larger particles are generally more aged than smaller ones (Sun et al., 2012; Xu et al., 2021).

The volume size distribution of factor 3 ranges from 40 nm to 500 nm, with a geometric mean diameter of approximately 240 nm, contributing 46% to the total volume concentration. It shows strong correlations with HOA ( $R = 0.89$ ), COA ( $R = 0.93$ ), and rBC ( $R = 0.92$ ). This finding aligns with previous studies, which indicate that the peak volume size for HOA, COA, and rBC from traffic emissions, typically occurs between 200 nm and 300 nm (Cai et al., 2020b; Sun et al., 2012; Xu et al., 2021; Li et al., 2023a). Furthermore, the correlation coefficient between the volume of factor 3 and the total mass concentrations of HOA, COA, and rBC reaches 0.95, suggesting that factor 3 is predominantly associated with primary aerosol emissions. In addition, both factors 4 and 5 exhibit smaller volume size distributions, collectively contributing 12% to the total volume in the 20 nm to 500 nm range. Although the volume contributions of factors 4 and 5 are generally minor, as shown in Fig. 2a, their diurnal volume variations (illustrated in Fig. S3) and correlations with primary HOA, COA, and rBC are consistently higher than their correlations with secondary species (Fig. 2b). This suggests that factors 4 and 5 are more likely linked to primary sources.

Moreover, the total volume concentrations of factors 3, 4, and 5 are generally consistent with the total volume derived from the mass concentrations of HOA, COA, and rBC (5.8 vs. 6.1  $\mu\text{m}^3/\text{cm}^3$ ). However, in 53% of cases, the volume concentrations of factor 3 exceed those derived from the measurements of HOA, COA, and rBC, indicating that factor 3 may sometimes include contributions from other secondary sources, despite primary sources being dominant in most instances. Additionally, as shown in Fig. 2a, while factors 3, 4, and 5 primarily contribute to the mass of aerosols with a diameter of 235 nm, factor 1 also plays a significant role. This suggests that both primary emissions

and secondary aerosol ~~formations~~formation influence variations in  $m_{r1064,235}$ . In contrast, variations in  $m_{r1064,400}$  are predominantly controlled by secondary aerosol sources, with primary emissions playing a much lesser role. The differing sources of aerosols at diameters of 235 nm and 400 nm, along with the distinct variation characteristics of  $m_{r1064,235}$  and  $m_{r1064,400}$ , may provide insights into  $m_r$  differences of POA and SOA.

Based on the PNSD PMF results, the volume contribution of factor 3 at a diameter of 235 nm ranges from below 1% to nearly 99%, with an average of 60%. In comparison, the volume contribution of factor 1 varies between nearly 0% and 93%, averaging around 30%. Fig.2c illustrates the variations of  $m_{r1064,235}$  as a function of the ratio between the total volume of POA and rBC and the total volume of factors 3, 4, and 5 (referred to as factor 345) under conditions where volume of factor 345 dominates at 235 nm (volume fraction greater than 75%). The results indicate that as the contributions of POA and rBC increase within factor 345,  $m_{r1064,235}$  decreases from approximately 1.49 to about 1.46 when their volume fraction exceeds 0.5, subsequently fluctuating within a narrow range ( $1.46 \pm 0.02$ ). This suggests that  $m_{r1064,POA}$  is likely substantially lower than 1.46, considering that other secondary species contribute more than 30% to aerosol volume at 235 nm under these conditions.

Both primary and secondary sources contribute to aerosols of 400 nm, however, volume fractions of factor 1 plus 2 at 400 nm varied between near zero and 99% with an average of 61%, demonstrating that aerosols at 400 nm composed primarily of SIA and SOA, thus variations in SOA and SIA mainly control changes in  $m_{r1064,400}$ . With regard to  $m_r$  values of AS and AN,  $m_r$  of AS is consistently reported as 1.53 (Tang, 1996;Stelson, 1990;Lide, 2004), while reported  $m_r$  values of AN varied in a relatively large range of 1.41 to 1.56 (Jarzemski et al., 2003;Lide, 2004;Ouimette and Flagan, 1982;Schuster et al., 2005;Zhang et al., 2012). However, known  $m_r$  values of AS and AN demonstrate that it is likely not the formation of SIA that has led to  $m_{r,400}$  to be as high as 1.58, and could most possibly result from SOA formations, and results of previous laboratory (Li et al., 2017) and field studies (Zhao et al., 2021a) suggested that SOA formations might enhance  $m_r$  to reach beyond 1.6. However, the direct subtraction of  $m_{r1064,SOA}$  with current measurements is quite challenging due to that the lack of size distribution measurements of aerosol chemical compositions. To give a glimpse into the influences of SOA, the variations of  $m_{r1064,400}$  under different mass ratios of SOA to SIA are shown in Fig.2d. It shows that on average,  $m_{r1064,400}$  indeed increases as a function of SOA fraction, confirming that the  $m_{r1064,SOA}$  is higher than those of SIA. Especially, the  $m_{r1064,400}$  showed obviously higher correlations with MOOA ( $R=0.25$ ) than with LOOA ( $R=-0.24$ ) (Fig.S11), demonstrating that the higher  $m_r$  of MOOA than LOOA, and the  $m_r$  of LOOA is likely close to those

of SIA on the basis of results shown in Figure.S8b. Results of a few existing field measurements supports the finding. For example, results of Aldhaif et al. (2018) suggested that  $m_{r,OA}$  were likely positively correlated with the O/C. Results of Liu et al. (2022) revealed much stronger scattering abilities of MOOA which likely cannot be solely explained by larger size of MOOA. Li et al. (2023e) Li et al. (2023b) established a semi-empirical model to predict the  $m_{r,OA}$  from O/C and H/C which was partly confirmed using their laboratory measurements. On the basis of this model and element ratios of OA factors,  $m_r$  values for retrieved HOA, COA, LOOA, and MOOA during the first campaign are 1.48, 1.48, 1.45, 1.63, respectively, which is partly consistent with the field finding of this research that  $m_{r,POA}$  has remarkable difference with  $m_{r,SOA}$  with  $m_r$  of MOOA is substantially higher, however, the  $m_r$  values for HOA, COA might be overestimated by the scheme of Li, et al. (2023e)-(2023b).

### 3.2 Optical Closure Confirm Remarkably higher $m_{r,SOA}$ than $m_{r,POA}$

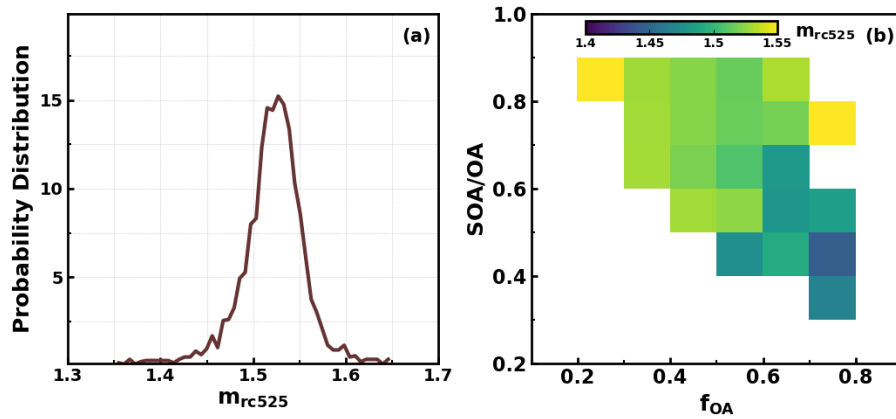


**Figure 3.** (a) Probability distribution of  $m_{rc525}$ ; (b) Variations of  $m_{rc525}$  under different OA mass fractions in NR-PM<sub>1</sub> ( $f_{OA}$ ) and SOA mass fractions in total OA (SOA/OA).

The probability distributions of retrieved  $m_{rc}$  using the optical closure method presented in Sect 2.3 is presented in Fig.3a,  $m_{rc525}$  generally ranges between 1.4 and 1.6 with an average of 1.52, which is close to the value of 1.53 typically used in optical closure studies on the basis of field measurements (Ma et al., 2011; Wexler and Clegg, 2002), and also generally consistent with the previously reported  $m_r$  range in Guangzhou (Zhang et al., 2016a). The retrieved  $m_{rc525}$  is a parameter that represents the bulk  $m_r$  of ambient aerosols, therefore, containing influences of both organic and inorganic components. To further reveal possible effects of POA and SOA on  $m_{rc525}$  variations, average  $m_{rc525}$  under different OA mass fractions in NR-PM<sub>1</sub> and SOA fractions in OA



435 are presented in Fig.3b. A general characteristic revealed that when OA accounts for more than 50%  
 436 of NR-PM<sub>1</sub>,  $m_{rc525}$  tends to be lower as mass fraction of POA increase, suggesting that increases in  
 437 POA would generally lower the  $m_{rc525}$ . The fact that  $m_{rc525}$  would be even lower than 1.45 when  
 438 POA dominates, suggesting that  $m_{rc525,POA}$  is likely lower than 1.45 which is consistent with the  
 439 finding revealed in Sect 3.1 that  $m_{r1064,POA}$  should be lower than 1.46. Results of Liu et al. (2013)  
 440 revealed that small  $m_r$  wavelength dependence of organic aerosols for wavelengths higher than 500  
 441 nm. The finding about  $m_{rc525,POA}$  and  $m_{r1064,POA}$  here demonstrates that both optical closure  
 442 calculations and DMA-SP2 measurements reveal same results on the value of  $m_{r,POA}$ . However, as  
 443 SOA dominates in OA, the  $m_{rc525}$  is enhanced to more than the average of 1.52, suggesting that the  
 444  $m_{rc525,SOA}$  is at least higher than 1.52 considering that  $m_{r525}$  of AS and AN is close to or lower than  
 445 1.52. These results qualitatively confirmed the finding in Sect 3.1 that  $m_{r,SOA}$  is substantially higher  
 446 than  $m_{r,POA}$ .

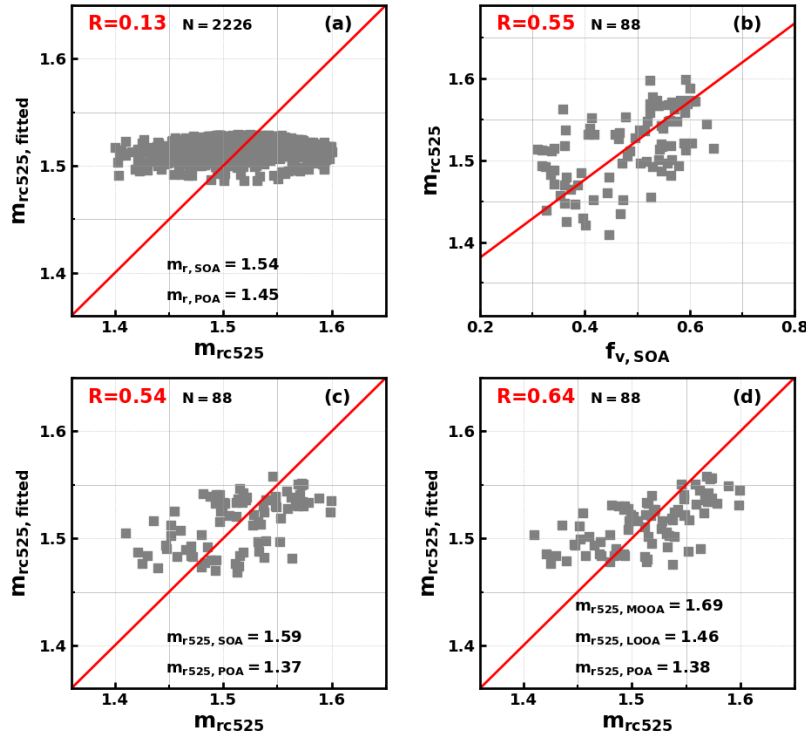


**Figure 4.** (a) Comparison between  $m_{rc525}$  and fitted  $m_{rc525}$  using the volume mixing rule, N is the sample number; (b) Relationships between  $m_{rc525}$  and volume fractions of SOA in NR-PM<sub>1</sub> ( $f_{v, SOA}$ ) when OA volume fractions in NR-PM<sub>1</sub> is higher than 75%; (c) Comparisons between  $m_{rc525}$  and fitted  $m_{rc525}$  for points in (b) using the volume mixing rule; (d) Comparisons between  $m_{rc525}$  and fitted  $m_{rc525}$  for points in (b) using the volume mixing rule, while LOOA and MOOA are treated separately.

The complex compositions of ambient aerosols and complex mixing states and refractive index mixing rule (Liu and Daum, 2008; Zhao et al., 2019a) result in the fact that retrieving  $m_{r, SOA}$  and  $m_{r, POA}$  on the basis of direct  $m_{rc525}$  measurements and aerosol composition measurements is extremely challenging (Zhao et al., 2022). Actually,  $m_{r, SOA}$  and  $m_{r, POA}$  are never reported on the basis of field measurements. Volume mixing rule was first applied in this study to all retrieved  $m_{rc525}$  points and corresponding aerosol chemical compositions to tentatively retrieve  $m_{rc525, SOA}$  and  $m_{rc525, POA}$ . The multilinear regression formula with the volume mixing rule could be expressed as

$$m_{r525} = \varepsilon_{AN} \times m_{rc525, AN} + \varepsilon_{AS} \times m_{rc525, AS} + \varepsilon_{POA} \times m_{rc525, POA} + \varepsilon_{SOA} \times m_{rc525, SOA} + \varepsilon_{AC} \times$$

456  $m_{rc525,AC}$ , where  $\varepsilon$  represents volume fraction of each species in total measured NR-PM<sub>1</sub>,  $\varepsilon_{AC}$   
 457 represents volume fraction of ammonium chloride by assuming all measured chloride mass is  
 458 ammonium chloride. In this formula, the  $m_{rc525,AS}$  and  $m_{rc525,AC}$  is set to 1.53 and  $m_{rc525,AN}$  is set to  
 459 1.5 (a middle value reported in the literatures) in the retrieval in terms of existing literatures as listed  
 460 in Sect 3.1. As shown in Fig.4a, if all retrieved  $m_{rc525}$  points were used,  $m_{rc525,POA}$  and  $m_{rc525,SOA}$  of  
 461 1.45 and 1.54 could be retrieved (using python curve\_fit function of module scipy.optimize). However,  
 462 it could be found that this rule could not reproduce observed large variations in  $m_{rc525}$ . It was realized  
 463 that the volume mixing rule would oversimplify the interactions in complex mixture with respect to  
 464 aerosol refractive index (Liu and Daum, 2008). This was confirmed by a few aerosol refractive index  
 465 studies (Zhao et al., 2019a).

466 If we focus on periods when OA dominates aerosol volume (OA volume in total NR-PM<sub>1</sub>  
 467 accounts for more than 75%),  $m_{rc525}$  shows clear [and](#) almost linear trend with the volume fractions of  
 468 SOA in NR-PM<sub>1</sub> as shown in Fig.4b. The question remains whether the volume mixing rule can be  
 469 used to retrieve  $m_{rc525}$  of POA and SOA from these organic aerosol-dominant points. The analysis

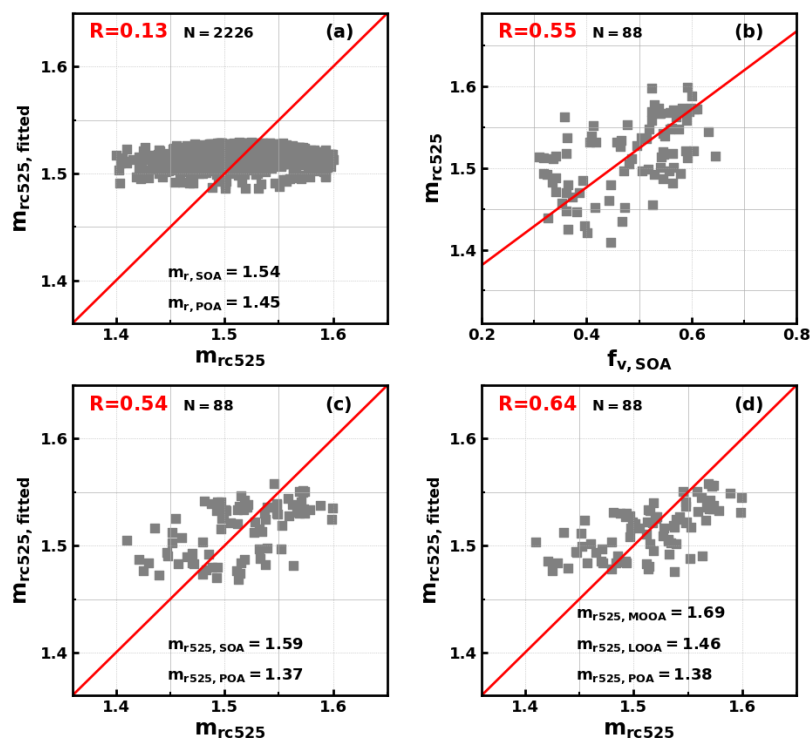


**Figure 4.** (a) Comparison between  $m_{rc525}$  and fitted  $m_{rc525}$  using the volume mixing rule, N is the sample number; (b) Relationships between  $m_{rc525}$  and volume fractions of SOA in NR-PM<sub>1</sub> ( $f_{v, SOA}$ ) when OA volume fractions in NR-PM<sub>1</sub> is higher than 75%; (c) Comparisons between  $m_{rc525}$  and fitted  $m_{rc525}$  for points in (b) using the volume mixing rule; (d) Comparisons between  $m_{rc525}$  and fitted  $m_{rc525}$  for points in (b) using the volume mixing rule, while LOOA and MOOA are treated separately. Red lines indicate the 1:1 reference lines.

in Sect. 3.1 demonstrates that the mass concentration of resolved PNSD factor that related with primary sources could mostly be explained by POA and BC, meaning that PNSD and of primary sources and secondary sources could be generally separated in the PMF procedure, suggesting that POA and SOA are likely prone to externally mixed. This could be explained by that the observation site is located near POA source regions in an urban area. This indicates that POA and SOA tend to be optically independent at the single-particle level. The optical test experiment introduced in Sect. S6 demonstrate that the volume mixing rule can generally be used to retrieve  $m_{rc525}$  of POA and SOA if aerosol particles of SOA and POA are externally mixed. In view of this, the volume mixing rule was further applied to scenarios when OA volume dominates (data points in Fig.4b), meaning that effects of other

chemical components are minimized. The overall  $m_{rc525}$  changes were captured by the fitting while retrieved values for  $m_{rc525,POA}$  and  $m_{rc525,SOA}$  are  $1.37 \pm 0.026$  and  $1.59 \pm 0.017$  as shown in Fig.4c. The relatively small uncertainty ranges for estimated  $m_{rc525,POA}$  and  $m_{rc525,SOA}$  confirms the quantitative difference between  $m_{rc525,POA}$  and  $m_{rc525,SOA}$ . For the average PNSD in the retrievals, increase  $m_{rc525}$  from 1.37 to 1.59 would result in an ~60% increase of aerosol scattering, which is significant for aerosol radiative forcing estimations (Kuang et al., 2015). Models that assume  $m_{r,POA}$  to 1.63 and  $m_{r,SOA}$  to 1.43 which is contrary to the finding here, would inevitably results significant bias in organic aerosol radiative forcing estimations (Curci et al., 2019). Based on the above analysis,  $m_{r,SOA}$  and  $m_{r,POA}$  of 1.37 and 1.59 might be better choice for model settings [in regions share similar emissions and meteorological conditions with the observation site](#).

Considering that O/C of LOOA and MOOA differ much (0.6 vs 1.27), ~~if~~ [during the long-term campaign. If](#) SOA was further treated separately as LOOA and MOOA in the fitting, extending the volume mixing rule formula as:  $m_{r525} = \varepsilon_{AN} \times m_{rc525,AN} + \varepsilon_{AS} \times m_{rc525,AS} + \varepsilon_{AC} \times m_{rc525,AC} + \varepsilon_{POA} \times m_{rc525,POA} + \varepsilon_{LOOA} \times m_{rc525,LOOA} + \varepsilon_{MOOA} \times m_{rc525,MOOA}$ , a better correlation coefficient could be achieved as shown in Fig.4d. Note that LOOA and MOOA are generally not externally mixed and likely be prone to internally mixed on the basis of knowledge about organic aerosol aging chain (Jimenez et al., 2009), therefore the volume mixing rule is likely not applicable, and the retrieved results serves better for qualitatively analysis. Retrieved  $m_{rc525,POA}$  of  $1.38 \pm 0.024$ , and retrieved  $m_{rc525,LOOA}$  and  $m_{rc525,MOOA}$  of  $1.46 \pm 0.069$  and  $1.69 \pm 0.059$ , consistent with the speculations in Sect 3.2 that  $m_{r,MOOA}$  is likely substantially higher than  $m_{r,LOOA}$  (Fig.S11), although significant retrieval bias of  $m_{rc525,LOOA}$  and  $m_{rc525,MOOA}$ . The retrieved  $m_{rc525,LOOA}$  and  $m_{rc525,MOOA}$  of 1.46 and 1.69 have a remarkable difference with those ( $m_{r,LOOA}$  and  $m_{r,MOOA}$  of 1.56 and 1.57) predicted with their O/C and H/C ratios as inputs of the scheme proposed by Li, et al. (2023c). ~~This result suggests that qualitatively,  $m_r$  increase with oxidation degree of SOA, which is contrary to results of most existing laboratory studies that increase of O/C would decrease  $m_r$  at the O/C range of LOOA and MOOA (2023b). This result suggests that qualitatively,  $m_r$  increase with oxidation degree of SOA. Previous laboratory results demonstrate that  $m_r$  could increase (Li et al., 2019; He et al., 2018; Moise et al., 2015, 2022). This is likely associated with that MOOA in Guangzhou urban area or decrease (He et al., 2018) with O/C depending on aerosol types, precursors and oxidation conditions. However, as summarized in Moise et al. (2015), most existing laboratory studies reveal that increase of O/C would decrease  $m_r$  at the O/C range of LOOA and MOOA of this study (0.6 to 1.27, and  $m_r$  from 1.46 to 1.69). This is likely associated with that MOOA in Guangzhou urban area is~~ mainly formed through

511 multiphase reactions (Zhai et al., 2023) thus has higher  $m_r$  as demonstrated by Li et al. (2017) that  
512 multiphase reactions enhance  $m_r$ , ~~while most~~. Most laboratory studies on evolution of  $m_{r,SOA}$  were  
513 conducted in the context of gas-phase reactions. However, for humid regions such as southern China,  
514 multiphase reactions likely prevail (Zhou et al., 2020; Xu et al., 2020).

#### 515 4 Conclusions

516 This study thoroughly leverages field measurements and multiple analytical techniques to  
517 constrain the real part of the scattering refractive index of organic aerosols. The results reveal  
518 substantially higher values for SOA compared to POA, helping to clarify a longstanding discrepancy  
519 in their optical properties. The  $m_r$  is a fundamental parameter for accurate simulations of aerosol  
520 optical properties and their roles in visibility degradation and direct aerosol radiative forcing. In  
521 addition, aerosol optical properties are also key for radiative flux simulations which are fundamental  
522 for atmospheric photochemistry (Tao et al., 2014; Tian et al., 2019). Therefore, results of studies have  
523 both significant implications in environmental and climate issues.

524 Results of Redemann et al. (2000) demonstrate that 5% variation in  $m_r$  can lead to approximately  
525 30% change in the radiative flux change at the top of atmosphere. Li et al. (2021) further demonstrated  
526 for  $m_{r,OA}$  changing from 1.3 to 1.65, stratospheric aerosol optical depth relatively changed from -20%  
527 to +50%, and caused up to  $\pm 100\%$  variability in shortwave radiative forcing, which matters more than  
528 mixing state. While OA are mainly composed of POA and SOA, and they both are major components  
529 of atmospheric aerosols, therefore accurate representations of  $m_{r,POA}$  and  $m_{r,SOA}$  are essential for  
530 accurate simulations of direct aerosol radiative effects whose uncertainties are the second largest  
531 contributions to overall climate forcing estimations (IPCC, AR6, 2023). Our long-term field  
532 observation results suggest that utilizing constant values for  $m_{r,OA}$  in models would lead to either  
533 significant underestimations or overestimations in scattering coefficient therefore significant  
534 deviations in estimations of direct aerosol radiative effects. The used constant value is another issue,  
535 as presented by Tsigaridis and Kanakidou (2018), most models use 1.53 as  $m_{r,OA}$  which is generally  
536 appropriate on the basis of this study if  $m_{r,OA}$  has to be assumed. While some models even use a  
537 constant, for example 1.45 for both SOA and POA which might cause systematical underestimation  
538 of OA scattering (Aouizerats et al., 2010; Ma et al., 2012b). If OA is further categorized into SOA and  
539 POA in models as applied in Curci, et al. (2019), the appropriate  $m_{r,POA}$  and  $m_{r,SOA}$  should be used.  
540 Large bias would be expected if  $m_{r,POA}$  and  $m_{r,SOA}$  are set to 1.63 and 1.43 as those in Curci, et al.  
541 (2019). In addition, in most models, element ratios of organic components are not available, and  
542 organic aerosols are generally categorized as several types of POA and SOA, and SOA are generally

543 treated as a whole in these models (Zhang et al., 2023; Pöhlker et al., 2023). Therefore,  $m_{r,POA}$  and  
544  $m_{r,SOA}$  values of 1.37 and 1.59 retrieved at 525 nm in this study are recommended for ~~model~~  
545 ~~settings~~ [regions share similar emissions and meteorological conditions with the observation site](#).

546 It should be noteworthy that the POA in this study are primarily composed of fossil combustion  
547 [from traffic](#) and cooking related organic aerosols, however, organic aerosols directly emitted from  
548 biomass burning (BBOA) [and other fossil combustions sources such as coal burning](#) also represent a  
549 major POA source. Mathai et al. (2023) reported  $m_r$  of homogeneously and inhomogeneously mixed  
550 tar balls in the free troposphere from biomass burnings as 1.26 and 1.4, which is close to the  
551 recommended  $m_{r,POA}$ . However, results of Womack et al. (2021) reported that  $m_r$  of biomass burning  
552 aerosols at 475 nm could be higher than 1.6. Results of Luo et al. (2022) further demonstrated that  $m_r$   
553 of BBOA might vary a lot and depends highly on combustion conditions. Accurate representations of  
554  $m_{r,BBOA}$  stand as urgent need, considering the increasing trends of biomass burning events under  
555 background of current global warming. However, the biggest challenge lies in accurate representations  
556 of organic aerosols  $m_r$  due to  $m_{r,SOA}$  variations, because SOA could be formed through varying  
557 pathways ([condensational growth or multiphase reactions](#)) of different precursor sources volatile  
558 organic compounds (biogenic versus anthropogenic), and existing results already proved that SOA  
559 formed from varying precursors and pathways has distinct  $m_r$ . Therefore, recommend value of  $m_{r,SOA}$   
560 in this study might represent more the  $m_r$  of SOA that formed from anthropogenic precursors in urban  
561 [and humid](#) regions. Overall, results of this study, underscore the substantially higher  $m_{r,SOA}$  than  
562  $m_{r,POA}$ , not the case currently assumed in models.

563 In addition, results of this study imply that  $m_r$  likely increased oxidation level, suggesting crucial  
564 impacts of SOA formation mechanisms on  $m_r$  variations. Future studies should further examine  
565 variations and evolution of  $m_{r,SOA}$  than  $m_{r,POA}$  under different emissions characteristics and  
566 chemistry pathways for reducing uncertainties of direct aerosol radiative effects simulations in  
567 chemical, weather and climate models.

568

569

570

571

572

573

574  
575  
576  
577  
578  
579  
580  
581  
582  
583  
584  
585  
586  
587  
588  
589  
590  
591

**Competing interests.** The contact author has declared that none of the authors has any competing interests.

**Data Availability.** All data presented in Figures of this manuscript are freely available at <https://doi.org/10.5281/zenodo.15786937>, and more specific raw data will be made available on request due to the data restriction policy.

**Author Contributions.** YK and LL designed the two field campaigns. YK conceived and led this research. LL, BL, JLS, HX, GZ, FLY, MMZ, FL and YK performed measurements of aerosol physical and chemical properties. TD and XD supported this campaign. JLS performed the analysis with YK and LL, JLS and YK wrote the manuscript. All authors contributed to revisions of this paper.

**Financial support.** This work is supported by National Natural Science Foundation of China (42175083, 42105092), the [Guangdong Basic and Applied Basic Research Foundation \(2025A1515011641\)](#) and Fundamental Research Funds for the Central Universities.



- 593 Aldhaif, A. M., Stahl, C., Braun, R. A., Moghaddam, M. A., Shingler, T., Crosbie, E., Sawamura, P.,  
 594 Dadashazar, H., Ziemba, L., Jimenez, J. L., Campuzano-Jost, P., and Sorooshian, A.: Characterization  
 595 of the Real Part of Dry Aerosol Refractive Index Over North America From the Surface to 12 km,  
 596 *Journal of Geophysical Research: Atmospheres*, 123, 8283-8300,  
 597 <https://doi.org/10.1029/2018JD028504>, 2018.
- 598 Aouizerats, B., Thouron, O., Tulet, P., Mallet, M., Gomes, L., and Henzing, J. S.: Development of an  
 599 online radiative module for the computation of aerosol optical properties in 3-D atmospheric models:  
 600 validation during the EUCAARI campaign, *Geosci. Model Dev.*, 3, 553-564, 10.5194/gmd-3-553-  
 601 2010, 2010.
- 602 Benko, D., Molnár, A., and Imre, K.: Study on the size dependence of complex refractive index of  
 603 atmospheric aerosol particles over Central Europe, *IDOJARAS*, 113, 157-175, 2009.
- 604 Bohren, C. F., and Huffman, D. R.: Absorption and Scattering by a Sphere, in: *Absorption and*  
 605 *Scattering of Light by Small Particles*, 82-129, 1998.
- 606 Cai, J., Chu, B., Yao, L., Yan, C., Heikkinen, L. M., Zheng, F., Li, C., Fan, X., Zhang, S., Yang, D.,  
 607 Wang, Y., Kokkonen, T. V., Chan, T., Zhou, Y., Dada, L., Liu, Y., He, H., Paasonen, P., Kujansuu, J.  
 608 T., Petäjä, T., Mohr, C., Kangasluoma, J., Bianchi, F., Sun, Y., Croteau, P. L., Worsnop, D. R.,  
 609 Kerminen, V.-M., Du, W., Kulmala, M., and Daellenbach, K. R.: Size-segregated particle number and  
 610 mass concentrations from different emission sources in urban Beijing, *Atmospheric Chemistry and*  
 611 *Physics*, 20, 12721-12740, 10.5194/acp-20-12721-2020, 2020a.
- 612 Cai, J., Chu, B., Yao, L., Yan, C., Heikkinen, L. M., Zheng, F., Li, C., Fan, X., Zhang, S., Yang, D.,  
 613 Wang, Y., Kokkonen, T. V., Chan, T., Zhou, Y., Dada, L., Liu, Y., He, H., Paasonen, P., Kujansuu, J.  
 614 T., Petäjä, T., Mohr, C., Kangasluoma, J., Bianchi, F., Sun, Y., Croteau, P. L., Worsnop, D. R.,  
 615 Kerminen, V. M., Du, W., Kulmala, M., and Daellenbach, K. R.: Size-segregated particle number and  
 616 mass concentrations from different emission sources in urban Beijing, *Atmos. Chem. Phys.*, 20, 12721-  
 617 12740, 10.5194/acp-20-12721-2020, 2020b.
- 618 Canonaco, F., Crippa, M., Slowik, J. G., Baltensperger, U., and Prévôt, A. S. H.: SoFi, an IGOR-based  
 619 interface for the efficient use of the generalized multilinear engine (ME-2) for the source  
 620 apportionment: ME-2 application to aerosol mass spectrometer data, *Atmos. Meas. Tech.*, 6, 3649-  
 621 3661, 10.5194/amt-6-3649-2013, 2013.
- 622 Canonaco, F., Tobler, A., Chen, G., Sosedova, Y., Slowik, J. G., Bozzetti, C., Daellenbach, K. R., El  
 623 Haddad, I., Crippa, M., Huang, R. J., Furger, M., Baltensperger, U., and Prévôt, A. S. H.: A new  
 624 method for long-term source apportionment with time-dependent factor profiles and uncertainty  
 625 assessment using SoFi Pro: application to 1 year of organic aerosol data, *Atmos. Meas. Tech.*, 14, 923-  
 626 943, 10.5194/amt-14-923-2021, 2021.
- 627 Cheng, Y. F., Berghof, M., Garland, R. M., Wiedensohler, A., Wehner, B., Müller, T., Su, H., Zhang,  
 628 Y. H., Achtert, P., Nowak, A., Pöschl, U., Zhu, T., Hu, M., and Zeng, L. M.: Influence of soot mixing  
 629 state on aerosol light absorption and single scattering albedo during air mass aging at a polluted  
 630 regional site in northeastern China, *Journal of Geophysical Research: Atmospheres*, 114,  
 631 <https://doi.org/10.1029/2008JD010883>, 2009.
- 632 Curci, G., Alyuz, U., Barò, R., Bianconi, R., Bieser, J., Christensen, J. H., Colette, A., Farrow, A.,  
 633 Francis, X., Jiménez-Guerrero, P., Im, U., Liu, P., Manders, A., Palacios-Peña, L., Prank, M., Pozzoli,  
 634 L., Sokhi, R., Solazzo, E., Tuccella, P., Unal, A., Vivanco, M. G., Hogrefe, C., and Galmarini, S.:  
 635 Modelling black carbon absorption of solar radiation: combining external and internal mixing  
 636 assumptions, *Atmos. Chem. Phys.*, 19, 181-204, 10.5194/acp-19-181-2019, 2019.
- 637 Drinovec, L., Močnik, G., Zotter, P., Prévôt, A. S. H., Ruckstuhl, C., Coz, E., Rupakheti, M., Sciare,  
 638 J., Müller, T., Wiedensohler, A., and Hansen, A. D. A.: The "dual-spot" Aethalometer: an improved  
 639 measurement of aerosol black carbon with real-time loading compensation, *Atmospheric*  
 640 *Measurement Techniques*, 8, 1965-1979, 10.5194/amt-8-1965-2015, 2015.

带格式的: 段落间距段前: 0 磅

Guo, J., Zhou, S., Cai, M., Zhao, J., Song, W., Zhao, W., Hu, W., Sun, Y., He, Y., Yang, C., Xu, X., Zhang, Z., Cheng, P., Fan, Q., Hang, J., Fan, S., Wang, X., and Wang, X.: Characterization of submicron particles by time-of-flight aerosol chemical speciation monitor (ToF-ACSM) during wintertime: aerosol composition, sources, and chemical processes in Guangzhou, China, *Atmospheric Chemistry and Physics*, 20, 7595-7615, 10.5194/acp-20-7595-2020, 2020.

He, Q., Bluvshstein, N., Segev, L., Meidan, D., Flores, J. M., Brown, S. S., Brune, W., and Rudich, Y.: Evolution of the Complex Refractive Index of Secondary Organic Aerosols during Atmospheric Aging, *Environmental science & technology*, 52, 3456-3465, 10.1021/acs.est.7b05742, 2018.

He, Q., Li, C., Siemens, K., Morales, A. C., Hettiyadura, A. P. S., Laskin, A., and Rudich, Y.: [Optical Properties of Secondary Organic Aerosol Produced by Photooxidation of Naphthalene under NOx Condition](#), *Environmental science & technology*, 56, 4816-4827, 10.1021/acs.est.1c07328, 2022.

Hoffer, A., Tóth, Á., Pósfai, M., Chung, C. E., and Gelencsér, A.: Brown carbon absorption in the red and near-infrared spectral region, *Atmos. Meas. Tech.*, 10, 2353-2359, 10.5194/amt-10-2353-2017, 2017.

IPCC, AR6: The Earth's Energy Budget, Climate Feedbacks and Climate Sensitivity, in: *Climate Change 2021 – The Physical Science Basis: Working Group I Contribution to the Sixth Assessment Report of the Intergovernmental Panel on Climate Change*, edited by: Intergovernmental Panel on Climate, C., Cambridge University Press, Cambridge, 923-1054, 2023.

Jarzembski, M. A., Norman, M. L., Fuller, K. A., Srivastava, V., and Cutten, D. R.: Complex refractive index of ammonium nitrate in the 2–20- $\mu$ m spectral range, *Appl. Opt.*, 42, 922-930, 10.1364/AO.42.000922, 2003.

Jimenez, J. L., Canagaratna, M. R., Donahue, N. M., Prevot, A. S. H., Zhang, Q., Kroll, J. H., DeCarlo, P. F., Allan, J. D., Coe, H., Ng, N. L., Aiken, A. C., Docherty, K. S., Ulbrich, I. M., Grieshop, A. P., Robinson, A. L., Duplissy, J., Smith, J. D., Wilson, K. R., Lanz, V. A., Hueglin, C., Sun, Y. L., Tian, J., Laaksonen, A., Raatikainen, T., Rautiainen, J., Vaattovaara, P., Ehn, M., Kulmala, M., Tomlinson, J. M., Collins, D. R., Cubison, M. J., Dunlea, J., Huffman, J. A., Onasch, T. B., Alfarra, M. R., Williams, P. I., Bower, K., Kondo, Y., Schneider, J., Drewnick, F., Borrmann, S., Weimer, S., Demerjian, K., Salcedo, D., Cottrell, L., Griffin, R., Takami, A., Miyoshi, T., Hatakeyama, S., Shimono, A., Sun, J. Y., Zhang, Y. M., Dzepina, K., Kimmel, J. R., Sueper, D., Jayne, J. T., Herndon, S. C., Trimborn, A. M., Williams, L. R., Wood, E. C., Middlebrook, A. M., Kolb, C. E., Baltensperger, U., and Worsnop, D. R.: Evolution of Organic Aerosols in the Atmosphere, *Science*, 326, 1525-1529, 10.1126/science.1180353, 2009.

Kanakidou, M., Seinfeld, J. H., Pandis, S. N., Barnes, I., Dentener, F. J., Facchini, M. C., Van Dingenen, R., Ervens, B., Nenes, A., Nielsen, C. J., Swietlicki, E., Putaud, J. P., Balkanski, Y., Fuzzi, S., Horth, J., Moortgat, G. K., Winterhalter, R., Myhre, C. E. L., Tsigaridis, K., Vignati, E., Stephanou, E. G., and Wilson, J.: Organic aerosol and global climate modelling: a review, *Atmos. Chem. Phys.*, 5, 1053-1123, 10.5194/acp-5-1053-2005, 2005.

Kim, H., Liu, S., Russell, L. M., and Paulson, S. E.: Dependence of Real Refractive Indices on O:C, H:C and Mass Fragments of Secondary Organic Aerosol Generated from Ozonolysis and Photooxidation of Limonene and  $\alpha$ -Pinene, *Aerosol Science and Technology*, 48, 498-507, 10.1080/02786826.2014.893278, 2014.

Kuang, Y., Zhao, C. S., Tao, J. C., and Ma, N.: Diurnal variations of aerosol optical properties in the North China Plain and their influences on the estimates of direct aerosol radiative effect, *Atmos. Chem. Phys.*, 15, 5761-5772, 10.5194/acp-15-5761-2015, 2015.

Kuang, Y., Zhao, C. S., Zhao, G., Tao, J. C., Xu, W., Ma, N., and Bian, Y. X.: A novel method for calculating ambient aerosol liquid water content based on measurements of a humidified nephelometer system, *Atmospheric Measurement Techniques*, 11, 2967-2982, 10.5194/amt-11-2967-2018, 2018.

Kuang, Y., Huang, S., Xue, B., Luo, B., Song, Q., Chen, W., Hu, W., Li, W., Zhao, P., Cai, M., Peng, Y., Qi, J., Li, T., Wang, S., Chen, D., Yue, D., Yuan, B., and Shao, M.: Contrasting effects of secondary

带格式的: 段落间距段前: 0 磅

organic aerosol formations on organic aerosol hygroscopicity, *Atmos. Chem. Phys.*, 21, 10375-10391, 10.5194/acp-21-10375-2021, 2021.

Kuang, Y., Xu, W., Tao, J., Luo, B., Liu, L., Xu, H., Xu, W., Xue, B., Zhai, M., Liu, P., and Sun, Y.: Divergent Impacts of Biomass Burning and Fossil Fuel Combustion Aerosols on Fog-Cloud Microphysics and Chemistry: Novel Insights From Advanced Aerosol-Fog Sampling, *Geophysical Research Letters*, 51, e2023GL107147, <https://doi.org/10.1029/2023GL107147>, 2024.

Lambe, A. T., Cappa, C. D., Massoli, P., Onasch, T. B., Forestieri, S. D., Martin, A. T., Cummings, M. J., Croasdale, D. R., Brune, W. H., Worsnop, D. R., and Davidovits, P.: Relationship between Oxidation Level and Optical Properties of Secondary Organic Aerosol, *Environmental science & technology*, 47, 6349-6357, 10.1021/es401043j, 2013.

Li, C., He, Q., Schade, J., Passig, J., Zimmermann, R., Meidan, D., Laskin, A., and Rudich, Y.: Dynamic changes in optical and chemical properties of tar ball aerosols by atmospheric photochemical aging, *Atmos. Chem. Phys.*, 19, 139-163, 10.5194/acp-19-139-2019, 2019.

Li, F., Luo, B., Zhai, M., Liu, L., Zhao, G., Xu, H., Deng, T., Deng, X., Tan, H., Kuang, Y., and Zhao, J.: Black carbon content of traffic emissions significantly impacts black carbon mass size distributions and mixing states, *Atmos. Chem. Phys.*, 23, 6545-6558, 10.5194/acp-23-6545-2023, 2023a.

Li, K., Li, J., Liggio, J., Wang, W., Ge, M., Liu, Q., Guo, Y., Tong, S., Li, J., Peng, C., Jing, B., Wang, D., and Fu, P.: Enhanced Light Scattering of Secondary Organic Aerosols by Multiphase Reactions, *Environmental Science & Technology*, 51, 1285-1292, 10.1021/acs.est.6b03229, 2017.

Li, Y., Dykema, J., Deshler, T., and Keutsch, F.: Composition Dependence of Stratospheric Aerosol Shortwave Radiative Forcing in Northern Midlatitudes, *Geophysical Research Letters*, 48, e2021GL094427, <https://doi.org/10.1029/2021GL094427>, 2021.

Li, Y., Bai, B., Dykema, J., Shin, N., Lambe, A. T., Chen, Q., Kuwata, M., Ng, N. L., Keutsch, F. N., and Liu, P.: Predicting Real Refractive Index of Organic Aerosols From Elemental Composition, *Geophysical Research Letters*, 50, e2023GL103446, <https://doi.org/10.1029/2023GL103446>, 2023b.

Li, Y., Bai, B., Dykema, J., Shin, N., Lambe, A. T., Chen, Q., Kuwata, M., Ng, N. L., Keutsch, F. N., and Liu, P.: Predicting Real Refractive Index of Organic Aerosols From Elemental Composition, *Geophysical Research Letters*, 50, e2023GL103446, <https://doi.org/10.1029/2023GL103446>, 2023c.

Lide, D. R.: CRC handbook of chemistry and physics, CRC press, 2004.

Liu, L., Kuang, Y., Zhai, M., Xue, B., He, Y., Tao, J., Luo, B., Xu, W., Tao, J., Yin, C., Li, F., Xu, H., Deng, T., Deng, X., Tan, H., and Shao, M.: Strong light scattering of highly oxygenated organic aerosols impacts significantly on visibility degradation, *Atmos. Chem. Phys.*, 22, 7713-7726, 10.5194/acp-22-7713-2022, 2022.

Liu, P., Zhang, Y., and Martin, S. T.: Complex Refractive Indices of Thin Films of Secondary Organic Materials by Spectroscopic Ellipsometry from 220 to 1200 nm, *Environmental science & technology*, 47, 13594-13601, 10.1021/es403411e, 2013.

Liu, Y., and Daum, P. H.: Relationship of refractive index to mass density and self-consistency of mixing rules for multicomponent mixtures like ambient aerosols, *Journal of Aerosol Science*, 39, 974-986, <https://doi.org/10.1016/j.jaerosci.2008.06.006>, 2008.

Luo, B., Kuang, Y., Huang, S., Song, Q., Hu, W., Li, W., Peng, Y., Chen, D., Yue, D., Yuan, B., and Shao, M.: Parameterizations of size distribution and refractive index of biomass burning organic aerosol with black carbon content, *Atmos. Chem. Phys.*, 22, 12401-12415, 10.5194/acp-22-12401-2022, 2022.

Müller, T., Laborde, M., Kassell, G., and Wiedensohler, A.: Design and performance of a three-wavelength LED-based total scatter and backscatter integrating nephelometer, *Atmos. Meas. Tech.*, 4, 1291-1303, 10.5194/amt-4-1291-2011, 2011.

带格式的: 段落间距段前: 0 磅

Ma, N., Zhao, C. S., Nowak, A., Müller, T., Pfeifer, S., Cheng, Y. F., Deng, Z. Z., Liu, P. F., Xu, W. Y., Ran, L., Yan, P., Göbel, T., Hallbauer, E., Mildenberger, K., Henning, S., Yu, J., Chen, L. L., Zhou, X. J., Stratmann, F., and Wiedensohler, A.: Aerosol optical properties in the North China Plain during HaChi campaign: an in-situ optical closure study, *Atmos. Chem. Phys.*, 11, 5959-5973, 10.5194/acp-11-5959-2011, 2011.

Ma, N., Zhao, C. S., Müller, T., Cheng, Y. F., Liu, P. F., Deng, Z. Z., Xu, W. Y., Ran, L., Nekat, B., van Pinxteren, D., Gnauk, T., Müller, K., Herrmann, H., Yan, P., Zhou, X. J., and Wiedensohler, A.: A new method to determine the mixing state of light absorbing carbonaceous using the measured aerosol optical properties and number size distributions, *Atmos. Chem. Phys.*, 12, 2381-2397, 10.5194/acp-12-2381-2012, 2012a.

Ma, X., Yu, F., and Luo, G.: Aerosol direct radiative forcing based on GEOS-Chem-APM and uncertainties, *Atmos. Chem. Phys.*, 12, 5563-5581, 10.5194/acp-12-5563-2012, 2012b.

Mathai, S., Veghte, D., Kovarik, L., Mazzoleni, C., Tseng, K.-P., Bucci, S., Capek, T., Cheng, Z., Marinoni, A., and China, S.: Optical Properties of Individual Tar Balls in the Free Troposphere, *Environmental science & technology*, 57, 16834-16842, 10.1021/acs.est.3c03498, 2023.

McMeeking, G. R., Kreidenweis, S. M., Carrico, C. M., Collett, J. L., Day, D. E., and Malm, W. C.: Observations of smoke-influenced aerosol during the Yosemite Aerosol Characterization Study: 2. Aerosol scattering and absorbing properties, *Journal of Geophysical Research: Atmospheres*, 110, 10.1029/2004jd005624, 2005.

Moise, T., Flores, J. M., and Rudich, Y.: Optical Properties of Secondary Organic Aerosols and Their Changes by Chemical Processes, *Chemical Reviews*, 115, 4400-4439, 10.1021/cr5005259, 2015.

Ouimette, J. R., and Flagan, R. C.: The extinction coefficient of multicomponent aerosols, *Atmospheric Environment* (1967), 16, 2405-2419, [https://doi.org/10.1016/0004-6981\(82\)90131-7](https://doi.org/10.1016/0004-6981(82)90131-7), 1982.

Pöhlker, M. L., Pöhlker, C., Quaas, J., Mülmenstädt, J., Pozzer, A., Andreae, M. O., Artaxo, P., Block, K., Coe, H., Ervens, B., Gallimore, P., Gaston, C. J., Gunthe, S. S., Henning, S., Herrmann, H., Krüger, O. O., McFiggans, G., Poulain, L., Raj, S. S., Reyes-Villegas, E., Royer, H. M., Walter, D., Wang, Y., and Pöschl, U.: Global organic and inorganic aerosol hygroscopicity and its effect on radiative forcing, *Nature communications*, 14, 6139, 10.1038/s41467-023-41695-8, 2023.

Qiao, H., Kuang, Y., Yuan, F., Liu, L., Zhai, M., Xu, H., Zou, Y., Deng, T., and Deng, X.: Unlocking the Mystery of Aerosol Phase Transitions Governed by Relative Humidity History Through an Advanced Outdoor Nephelometer System, *Geophysical Research Letters*, 51, e2023GL107179, <https://doi.org/10.1029/2023GL107179>, 2024.

Redemann, J., Turco, R. P., Liou, K. N., Hobbs, P. V., Hartley, W. S., Bergstrom, R. W., Browell, E. V., and Russell, P. B.: Case studies of the vertical structure of the direct shortwave aerosol radiative forcing during TARFOX, *Journal of Geophysical Research: Atmospheres*, 105, 9971-9979, <https://doi.org/10.1029/1999JD901042>, 2000.

Saleh, R.: From Measurements to Models: Toward Accurate Representation of Brown Carbon in Climate Calculations, *Current Pollution Reports*, 6, 90-104, 10.1007/s40726-020-00139-3, 2020.

Schuster, G. L., Dubovik, O., Holben, B. N., and Clothiaux, E. E.: Inferring black carbon content and specific absorption from Aerosol Robotic Network (AERONET) aerosol retrievals, *Journal of Geophysical Research: Atmospheres*, 110, <https://doi.org/10.1029/2004JD004548>, 2005.

[Schwarz, J. P., Gao, R. S., Fahey, D. W., Thomson, D. S., Watts, L. A., Wilson, J. C., Reeves, J. M., Darbeheshti, M., Baumgardner, D. G., Kok, G. L., Chung, S. H., Schulz, M., Hendricks, J., Lauer, A., Kärcher, B., Slowik, J. G., Rosenlof, K. H., Thompson, T. L., Langford, A. O., Loewenstein, M., and Aikin, K. C.: Single-particle measurements of midlatitude black carbon and light-scattering aerosols from the boundary layer to the lower stratosphere, \*Journal of Geophysical Research: Atmospheres\*, 111, D16207, 10.1029/2006JD007076, 2006.](#)

Stelson, A. W.: Urban aerosol refractive index prediction by partial molar refraction approach, *Environmental science & technology*, 24, 1676-1679, 1990.

带格式的: 段落间距段前: 0 磅

Sun, Y. L., Zhang, Q., Schwab, J. J., Yang, T., Ng, N. L., and Demerjian, K. L.: Factor analysis of combined organic and inorganic aerosol mass spectra from high resolution aerosol mass spectrometer measurements, *Atmos. Chem. Phys.*, 12, 8537-8551, 10.5194/acp-12-8537-2012, 2012.  
 Tang, I. N.: Chemical and size effects of hygroscopic aerosols on light scattering coefficients, *Journal of Geophysical Research: Atmospheres*, 101, 19245-19250, <https://doi.org/10.1029/96JD03003>, 1996.  
 Tao, J. C., Zhao, C. S., Ma, N., and Liu, P. F.: The impact of aerosol hygroscopic growth on the single-scattering albedo and its application on the NO<sub>2</sub> photolysis rate coefficient, *Atmos. Chem. Phys.*, 14, 12055-12067, 10.5194/acp-14-12055-2014, 2014.  
 Tian, R., Ma, X., Jia, H., Yu, F., Sha, T., and Zan, Y.: Aerosol radiative effects on tropospheric photochemistry with GEOS-Chem simulations, *Atmospheric Environment*, 208, 82-94, <https://doi.org/10.1016/j.atmosenv.2019.03.032>, 2019.  
 Tsigaridis, K., and Kanakidou, M.: The Present and Future of Secondary Organic Aerosol Direct Forcing on Climate, *Current Climate Change Reports*, 4, 84-98, 10.1007/s40641-018-0092-3, 2018.  
 Wexler, A. S., and Clegg, S. L.: Atmospheric aerosol models for systems including the ions H<sup>+</sup>, NH<sub>4</sub><sup>+</sup>, Na<sup>+</sup>, SO<sub>4</sub><sup>2-</sup>, NO<sub>3</sub><sup>-</sup>, Cl<sup>-</sup>, Br<sup>-</sup>, and H<sub>2</sub>O, *Journal of Geophysical Research: Atmospheres*, 107, ACH 14-11-ACH 14-14, 10.1029/2001jd000451, 2002.  
 Womack, C. C., Manfred, K. M., Wagner, N. L., Adler, G., Franchin, A., Lamb, K. D., Middlebrook, A. M., Schwarz, J. P., Brock, C. A., Brown, S. S., and Washenfelder, R. A.: Complex refractive indices in the ultraviolet and visible spectral region for highly absorbing non-spherical biomass burning aerosol, *Atmos. Chem. Phys.*, 21, 7235-7252, 10.5194/acp-21-7235-2021, 2021.  
 Wu, Y., Li, J., Xia, Y., Deng, Z., Tao, J., Tian, P., Gao, Z., Xia, X., and Zhang, R.: Size-resolved refractive index of scattering aerosols in urban Beijing: A seasonal comparison, *Aerosol Science and Technology*, 55, 1070-1083, 10.1080/02786826.2021.1924357, 2021.  
 Xu, W., Kuang, Y., Bian, Y., Liu, L., Li, F., Wang, Y., Xue, B., Luo, B., Huang, S., Yuan, B., Zhao, P., and Shao, M.: Current Challenges in Visibility Improvement in Southern China, *Environmental Science & Technology Letters*, 7, 395-401, 10.1021/acs.estlett.0c00274, 2020.  
 Xu, W., Chen, C., Qiu, Y., Xie, C., Chen, Y., Ma, N., Xu, W., Fu, P., Wang, Z., Pan, X., Zhu, J., Ng, N. L., and Sun, Y.: Size-resolved characterization of organic aerosol in the North China Plain: new insights from high resolution spectral analysis, *Environmental Science: Atmospheres*, 1, 346-358, 10.1039/d1ea00025j, 2021.  
 Yuan, J. F., Huang, X. F., Cao, L. M., Cui, J., Zhu, Q., Huang, C. N., Lan, Z. J., and He, L. Y.: Light absorption of brown carbon aerosol in the PRD region of China, *Atmos. Chem. Phys.*, 16, 1433-1443, 10.5194/acp-16-1433-2016, 2016.  
 Zhai, M., Kuang, Y., Liu, L., He, Y., Luo, B., Xu, W., Tao, J., Zou, Y., Li, F., Yin, C., Li, C., Xu, H., and Deng, X.: Insights into characteristics and formation mechanisms of secondary organic aerosols in the Guangzhou urban area, *Atmos. Chem. Phys.*, 23, 5119-5133, 10.5194/acp-23-5119-2023, 2023.  
 Zhang, G., Bi, X., Qiu, N., Han, B., Lin, Q., Peng, L., Chen, D., Wang, X., Peng, P., amp, apos, an, Sheng, G., and Zhou, Z.: The real part of the refractive indices and effective densities for chemically segregated ambient aerosols in Guangzhou measured by a single-particle aerosol mass spectrometer, *Atmospheric Chemistry and Physics*, 16, 2631-2640, 10.5194/acp-16-2631-2016, 2016a.  
 Zhang, H., Shen, Z., Wei, X., Zhang, M., and Li, Z.: Comparison of optical properties of nitrate and sulfate aerosol and the direct radiative forcing due to nitrate in China, *Atmospheric Research*, 113, 113-125, <https://doi.org/10.1016/j.atmosres.2012.04.020>, 2012.  
 Zhang, Q., Jimenez, J. L., Canagaratna, M. R., Allan, J. D., Coe, H., Ulbrich, I., Alfarra, M. R., Takami, A., Middlebrook, A. M., Sun, Y. L., Dzepina, K., Dunlea, E., Docherty, K., DeCarlo, P. F., Salcedo, D., Onasch, T., Jayne, J. T., Miyoshi, T., Shimojo, A., Hatakeyama, S., Takegawa, N., Kondo, Y., Schneider, J., Drewnick, F., Borrmann, S., Weimer, S., Demerjian, K., Williams, P., Bower, K., Bahreini, R., Cottrell, L., Griffin, R. J., Rautiainen, J., Sun, J. Y., Zhang, Y. M., and Worsnop, D. R.: Ubiquity and dominance of oxygenated species in organic aerosols in anthropogenically-influenced

带格式的: 段落间距段前: 0 磅



838 Northern Hemisphere midlatitudes, *Geophysical Research Letters*, 34, n/a-n/a,  
839 10.1029/2007GL029979, 2007.

840 Zhang, S., Shen, X., Sun, J., Zhang, Y., Zhang, X., Xia, C., Hu, X., Zhong, J., Wang, J., and Liu, S.:  
841 Atmospheric Particle Hygroscopicity and the Influence by Oxidation State of Organic Aerosols in  
842 Urban Beijing, *Journal of Environmental Sciences*, 124, 544-556,  
843 <https://doi.org/10.1016/j.jes.2021.11.019>, 2023.

844 Zhang, Y., Zhang, Q., Cheng, Y., Su, H., Kecorius, S., Wang, Z., Wu, Z., Hu, M., Zhu, T.,  
845 Wiedensohler, A., and He, K.: Measuring the morphology and density of internally mixed black carbon  
846 with SP2 and VTDMA: new insight into the absorption enhancement of black carbon in the atmosphere,  
847 *Atmospheric Measurement Techniques*, 9, 1833-1843, 10.5194/amt-9-1833-2016, 2016b.

848 Zhao, G., Tan, T., Zhao, W., Guo, S., Tian, P., and Zhao, C.: A new parameterization scheme for the  
849 real part of the ambient urban aerosol refractive index, *Atmos. Chem. Phys.*, 19, 12875-12885,  
850 10.5194/acp-19-12875-2019, 2019a.

851 Zhao, G., Tao, J., Kuang, Y., Shen, C., Yu, Y., and Zhao, C.: Role of black carbon mass size  
852 distribution in the direct aerosol radiative forcing, *Atmos. Chem. Phys.*, 19, 13175-13188,  
853 10.5194/acp-19-13175-2019, 2019b.

854 Zhao, G., Zhao, W., and Zhao, C.: Method to measure the size-resolved real part of aerosol refractive  
855 index using differential mobility analyzer in tandem with single-particle soot photometer, *Atmos.*  
856 *Meas. Tech.*, 12, 3541-3550, 10.5194/amt-12-3541-2019, 2019c.

857 Zhao, G., Li, F., and Zhao, C.: Determination of the refractive index of ambient aerosols, *Atmospheric*  
858 *Environment*, 240, 117800, 10.1016/j.atmosenv.2020.117800, 2020.

859 Zhao, G., Hu, M., Fang, X., Tan, T., Xiao, Y., Du, Z., Zheng, J., Shang, D., Wu, Z., Guo, S., and Zhao,  
860 C.: Larger than expected variation range in the real part of the refractive index for ambient aerosols in  
861 China, *Science of The Total Environment*, 779, 146443,  
862 <https://doi.org/10.1016/j.scitotenv.2021.146443>, 2021a.

863 Zhao, G., Hu, M., Zhu, W., Tan, T., Shang, D., Zheng, J., Du, Z., Guo, S., Wu, Z., Zeng, L., and Zhao,  
864 C.: Parameterization of the ambient aerosol refractive index with source appointed chemical  
865 compositions, *Science of The Total Environment*, 842, 156573,  
866 <https://doi.org/10.1016/j.scitotenv.2022.156573>, 2022.

867 Zhao, W., Tan, W., Zhao, G., Shen, C., Yu, Y., and Zhao, C.: Determination of equivalent black carbon  
868 mass concentration from aerosol light absorption using variable mass absorption cross section, *Atmos.*  
869 *Meas. Tech.*, 14, 1319-1331, 10.5194/amt-14-1319-2021, 2021b.

870 Zhong, J., Zhang, X., Wang, Y., Wang, J., Shen, X., Zhang, H., Wang, T., Xie, Z., Liu, C., Zhang, H.,  
871 Zhao, T., Sun, J., Fan, S., Gao, Z., Li, Y., and Wang, L.: The two-way feedback mechanism between  
872 unfavorable meteorological conditions and cumulative aerosol pollution in various haze regions of  
873 China, *Atmos. Chem. Phys.*, 19, 3287-3306, 10.5194/acp-19-3287-2019, 2019.

874 Zhou, Y., Ma, N., Wang, Q., Wang, Z., Chen, C., Tao, J., Hong, J., Peng, L., He, Y., Xie, L., Zhu, S.,  
875 Zhang, Y., Li, G., Xu, W., Cheng, P., Kuhn, U., Zhou, G., Fu, P., Zhang, Q., Su, H., and Cheng, Y.:  
876 Bimodal distribution of size-resolved particle effective density: results from a short campaign in a rural  
877 environment over the North China Plain, *Atmos. Chem. Phys.*, 22, 2029-2047, 10.5194/acp-22-2029-  
878 2022, 2022.

879 W., Xu, W., Kim, H., Zhang, Q., Fu, P., Worsnop, D. R., and Sun, Y.: A review of aerosol  
880 chemistry in Asia: insights from aerosol mass spectrometer measurements, *Environmental Science:  
881 Processes & Impacts*, 22, 1616-1653, 10.1039/D0EM00212G, 2020.

881 Zhou, Y., Ma, N., Wang, Q., Wang, Z., Chen, C., Tao, J., Hong, J., Peng, L., He, Y., Xie, L., Zhu, S.,  
882 Zhang, Y., Li, G., Xu, W., Cheng, P., Kuhn, U., Zhou, G., Fu, P., Zhang, Q., Su, H., and Cheng, Y.:  
883 Bimodal distribution of size-resolved particle effective density: results from a short campaign in a rural  
884 environment over the North China Plain, *Atmos. Chem. Phys.*, 22, 2029-2047, 10.5194/acp-22-2029-  
885 2022, 2022.